

Spectroscopic investigations of $\text{Eu}^{3+}:\text{Y}_2\text{SiO}_5$ for quantum memory applications

B. Lauritzen, N. Timoney, N. Gisin, and M. Afzelius*

Group of Applied Physics, University of Geneva, CH-1211 Geneva 4, Switzerland

H. de Riedmatten

*ICFO - Institut de Ciències Fotòniques, Mediterranean Technology Park, 08860 Castelldefels, Spain and**ICREA - Institució Catalana de Recerca i Estudis Avançats, Lluís Companys 23, 08010 Barcelona, Spain*

Y. Sun

*Department of Physics, The University of South Dakota, Vermillion, South Dakota 57069, USA and**Department of Physics, Montana State University, Bozeman, Montana 59717, USA*

R. M. Macfarlane

*Department of Physics, Montana State University, Bozeman, Montana 59717, USA and**IBM Almaden Research Center, San Jose, California 95120, USA*

R. L. Cone

Department of Physics, Montana State University, Bozeman, Montana 59717, USA

(Received 31 October 2011; published 14 March 2012)

Rare-earth-ion-doped solids are promising materials as light-matter interfaces for quantum applications. Europium doped into an yttrium orthosilicate crystal in particular has interesting coherence properties and a suitable ground-state energy-level structure for a quantum memory for light. In this paper we report on spectroscopic investigations of this material from the perspective of implementing an atomic frequency comb (AFC)-type quantum memory with spin-wave storage. For this goal we determine the order of the hyperfine levels in the 7F_0 ground state and 5D_0 excited state, and we measure the relative strengths of the optical transitions between these levels. We also apply spectral hole burning techniques in order to prepare the system as a well-defined Λ system, as required for further quantum memory experiments. Furthermore, we measure the optical Rabi frequency on one of the strongest hyperfine transitions, a crucial experimental parameter for the AFC protocol. From this we also obtain a value for the transition dipole moment which is consistent with that obtained from absorption measurements.

DOI: [10.1103/PhysRevB.85.115111](https://doi.org/10.1103/PhysRevB.85.115111)

PACS number(s): 78.20.-e, 78.47.nd, 32.70.Cs

I. INTRODUCTION

In recent years much progress has been made toward the implementation of quantum memories (QMs) for light.¹⁻⁴ These devices are essential ingredients for the so-called quantum repeater, which would allow the realization of quantum communication schemes at a range beyond today's distance limits.⁵⁻⁷ QMs have already been realized using a variety of different physical systems such as hot and cold atomic gases⁸⁻¹⁴ and rare earth (RE)-ion-doped solids.¹⁵⁻¹⁸

RE-ion-doped solids are interesting materials for quantum memory applications for a number of reasons.⁴ They possess very long optical and spin coherence times. In $\text{Pr}^{3+}:\text{Y}_2\text{SiO}_5$, for example, a hyperfine coherence time of up to 30 s has been demonstrated and light could be stopped using electromagnetically induced transparency (EIT) for times exceeding 1 s.^{19,20} These coherence times only require cooling to cryogenic temperatures (2–4 K) using a commercial cooling apparatus, while complicated trapping or laser cooling techniques are not required.

Another interesting property is the large optical bandwidth due to static inhomogeneous broadening induced by the crystal environment.⁴ Moreover, the shape of the inhomogeneously broadened line can be modified using spectral hole burning techniques that allow the creation of spectral features as

required by memory protocols such as atomic frequency combs (AFCs) or controlled reversible inhomogeneous broadening (CRIB).²¹⁻²⁵ The AFC protocol is particularly interesting due to its high temporal multimode capacity, which allows storage of trains of single-photon pulses. This property can lead to a significant speedup of the entanglement distribution rates in long-distance quantum repeater architectures.²⁶ Using the AFC scheme the storage of more than 10^3 classical pulses was demonstrated in $\text{Tm}^{3+}:\text{yttrium aluminum garnet}$ (YAG) and up to 64 pulses at the single-photon level could be stored in $\text{Nd}^{3+}:\text{Y}_2\text{SiO}_5$.^{27,28} More recently the first storage of entanglement in a solid-state QM^{17,18} was demonstrated using the AFC scheme.

The large number of stationary ions present in a crystal also provides high optical depths despite the relatively low oscillator strength of the RE ions. This is crucial for achieving high memory efficiencies. Experimentally memory efficiency of 70% has been achieved in $\text{Pr}^{3+}:\text{Y}_2\text{SiO}_5$ using a memory scheme based on CRIB,¹⁶ while memory efficiencies in the range 20–35% have been reached using the AFC protocol.^{18,29-31} It should be noted, however, that a memory exploiting all of these properties, i.e., an efficient memory with long storage times and a high multimode capacity at the same time, has not been achieved yet.

Light storage at the single-photon level in RE-ion-doped solids has so far reached storage times of a few microseconds with weak coherent states, and a few hundreds of nanoseconds with nonclassical light. A way to extend the storage times of AFC- or CRIB-type memories is to convert the optical coherence induced by the absorption of a single photon into a spin coherence, so-called spin-wave storage. In addition to providing longer storage time, spin-wave storage is required for the AFC protocol in order to improve the protocol from one producing a delay to one producing a memory with on-demand readout.²¹ To map light onto a spin coherence one requires two ground-state spin levels which are both coupled to an excited-state level, a so-called Λ system. Furthermore, for the preparation of the absorption structure, a third long-lived ground-state level is required as a shelving state for the population. Λ systems fulfilling this additional condition can be found in praseodymium-doped inorganic crystals. Coherent optical techniques requiring Λ systems such as EIT, stimulated Raman adiabatic passage, or AFC with spin-wave storage have already been successfully demonstrated in praseodymium-doped materials.^{32–36} (Note that in the rest of this paper we use the term Λ system to denote the coherently coupled three-level system plus the additional population shelving state.) The levels that make up the Λ system are hyperfine levels, where the hyperfine splitting into three levels in the ground and the excited states occurs due to the $I = 5/2$ nuclear spin of praseodymium. But in praseodymium the splittings are of the order of a few megahertz, which puts a low limit on the achievable optical bandwidth.

Another rare-earth element which could provide a Λ system is europium, which has two isotopes, $^{151}\text{Eu}^{3+}$ and $^{153}\text{Eu}^{3+}$. The isotopes occur with almost equal natural abundance, and each possesses a hyperfine structure similar to that of praseodymium.³⁷ However, the ground-state hyperfine level spacings in Y_2SiO_5 are about seven times larger for $^{153}\text{Eu}^{3+}$ than for Pr^{3+} , resulting in a larger memory bandwidth. So far optical spectroscopic studies on this material have been carried out using crystals with natural abundances of the two isotopes. Since the isotope shift has not been resolved within the inhomogeneous broadening, such measurements yield an average over the two isotopes. These results include an optical homogeneous linewidth of 122 Hz,³⁸ temperature and concentration studies of the homogeneous linewidth, spectral hole lifetime, and anisotropic absorption.³⁹ By also using rf excitation techniques some isotope-specific spectroscopic parameters have been measured. For instance the ground- and excited-state hyperfine splittings^{37,40} show that the splitting for $^{153}\text{Eu}^{3+}$ is more than twice as large as for $^{151}\text{Eu}^{3+}$. Also, the spin Hamiltonian⁴¹ and hyperfine coherence time of 15.5 ms (Ref. 42) have been measured for isotope $^{151}\text{Eu}^{3+}$.

Europium doped into Y_2SiO_5 was in fact the material employed in the first demonstration of the CRIB memory scheme.²⁵ The two-level version of the CRIB scheme used in that work requires the preparation of a narrow absorption peak in a wider transmission pit, using spectral hole burning techniques. But it does not require the more elaborate state preparation for isolating a well-defined Λ system as defined above, which is necessary for spin-wave storage. Experiments toward this goal have been carried out by Nilsson *et al.* in $\text{Eu}^{3+}:\text{Y}_2\text{SiO}_5$.⁴³ However, as the authors conclude, those

efforts did not lead to satisfactory results since the sample contained both isotopes whose level separations coincide for ions at the crystallographic site they used (site 2). In the context of light storage experiments in this material, it should also be noted that the potential for high-bandwidth optical data storage of classical pulses was already realized in this material.^{44,45}

In this paper we present spectroscopic measurements on isotopically pure $^{153}\text{Eu}^{3+}:\text{Y}_2\text{SiO}_5$. We determine the ordering of the hyperfine levels in the ground 7F_0 and excited 5D_0 states, which were not known from previous rf-excitation experiments. This information is crucial in order to set up the spectral hole burning sequences used for isolating a well-defined Λ system. We also estimate the relative hyperfine transition strengths of the $^7F_0 \rightarrow ^5D_0$ transition, using two different methods. Based on these results we identify Λ systems that are suitable for the implementation of the AFC protocol with spin-wave storage. We then present a spectral hole burning sequence that allows us to experimentally isolate one of these Λ systems. In addition we present measurements of the Rabi frequency on one of its transitions, allowing us to deduce its electric dipole transition moment.

II. MEASUREMENT TECHNIQUES

A. The $\text{Eu}^{3+}:\text{Y}_2\text{SiO}_5$ sample

Y_2SiO_5 belongs to the crystallographic group C_{2h}^6 . It is known as a host material that provides excellent coherence properties due to its low nuclear spin density.^{37–42} Yttrium ions are replaced by the dopant, in our case $^{153}\text{Eu}^{3+}$, at two different crystallographic sites with low symmetry. The exact site occupancy is unknown. The overall $^{153}\text{Eu}^{3+}$ doping level of our crystal is 1000 ppm. The $^{153}\text{Eu}^{3+}$ purity is 98.8%, which eliminates the possibility of $^{151}\text{Eu}^{3+}$ contributing to any of the spectra shown in this paper. All measurements presented here were carried out on the $^7F_0 \rightarrow ^5D_0$ transition of site 1, at a wavelength of 580.04 nm (in vacuum). Note that site 1 has the highest absorption coefficient.³⁹ Y_2SiO_5 has three mutually perpendicular optical extinction axes, labeled D_1 , D_2 , and b , respectively. The light is traveling in the direction of the b axis and its polarization is aligned along the D_1 axis to maximize the absorption.³⁹ The energy-level scheme of $^{153}\text{Eu}^{3+}:\text{Y}_2\text{SiO}_5$ is shown in Fig. 1.

The energy levels of the ground and the excited states of each individual ion are shifted by the environment present in the crystal (crystal field interaction). The magnitude of this interaction depends on the local position of each ion inside the host material. This leads to an inhomogeneous broadening of the absorption line, of approximately 650 MHz in our case. The optical depth $d = \alpha L$ of our crystal with a length of $L = 1$ cm was $d = 1.2$ at the center of the absorption line. Here α is the absorption coefficient of the material.

The hyperfine structure is hidden inside the inhomogeneously broadened line which makes the search for a Λ system difficult. A laser at a fixed frequency shone into the sample is thus in resonance with nine different classes of ions, i.e., all possible transitions between hyperfine levels, $|i/2\rangle_g \rightarrow |j/2\rangle_e$, where g and e denote the ground and the excited states, respectively, and $i, j = 1, 3, 5$.⁴⁶

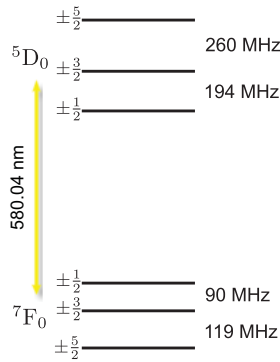


FIG. 1. (Color online) Hyperfine structures of the lowest crystal field levels of the ground 7F_0 and excited 5D_0 states of ${}^{153}\text{Eu}^{3+}:\text{Y}_2\text{SiO}_5$ (site 1). While the hyperfine energy differences have been measured by Yano *et al.*,^{37,40} the order of the hyperfine levels was determined in this work.

To obtain an optical Λ system we have to find transitions within the inhomogeneously broadened absorption line from two specific ground-state hyperfine levels that can each be efficiently coupled to the same excited-state hyperfine level. Furthermore, the strength of transitions involving the third ground-state level should be nonzero, since they are needed for the preparation of the absorption profile using hole burning techniques. As explained in Sec. III A, it is important that one only addresses the transitions of one of the nine classes mentioned above in order to have unique Rabi frequencies.

B. Spectral hole burning

For the investigation of the spectroscopic properties of materials with inhomogeneously broadened absorption lines one can use spectral hole burning techniques. Here we only briefly recall the basic ideas necessary to understand the spectral tailoring techniques used in this work. For the reader who is not familiar with the subject we refer also to Ref. 47.

Let us consider an inhomogeneously broadened ensemble of ions with three levels in the ground state. Let us further consider that the relaxation time between the ground-state levels T_1^{hyper} is much longer than the excited-state lifetime, $T_1^{\text{hyper}} \gg T_1^{\text{optical}}$. This is the case for $\text{Eu}^{3+}:\text{Y}_2\text{SiO}_5$ with a hyperfine relaxation time which can go beyond 20 days for temperatures around 2 K (Ref. 39) and an optical lifetime

of $T_1^{\text{optical}} = 2 \text{ ms}$.⁴⁰ Note that for our operation temperature of around 2.6 K we measured hyperfine relaxation times exceeding several hours, consistent with Ref. 39.

To begin, we consider only transitions involving one of the three excited-state levels. If a laser at a fixed frequency is shone into the sample, ions in resonance with the laser are excited and the absorption at the laser frequency will be reduced. This becomes visible in the form of a spectral hole in the absorption spectrum. The ions will deexcite into either of the three ground-state levels and they will accumulate in the levels not affected by the laser. The population in the initial level will decay toward zero with a sufficiently high number of pumping cycles. The spectral hole now persists for a time T_1^{hyper} . Furthermore, the absorption on the two transitions not addressed by the laser will be enhanced. This can be observed in the form of two peaks (so-called antiholes) in the absorption spectrum.

However, due to the inhomogeneous broadening the laser is actually in resonance with three different classes of ions involving the same excited-state hyperfine level. For all of the three possible hyperfine transitions there are ions whose energy levels are shifted by the crystal field such that they are in resonance with the laser. Therefore, for the simplified situation considered so far, there are six antiholes in addition to the central hole.

In practice, for ions like ${}^{153}\text{Eu}^{3+}$, the situation is further complicated because there are three hyperfine levels in the excited state. As already mentioned, there are nine different classes of ions in resonance with the laser, each on a different one of the nine possible optical-hyperfine transitions.⁴⁶ Hence there are in total 81 holes and antiholes, respectively, that may occur. They are symmetrically distributed around the central frequency and some of them can be found at identical frequencies. Figures 3(a) and 4 show examples of hole burning spectra. One can clearly see a range of holes and antiholes of different sizes distributed around the central hole at $\omega_{\text{pump}} = 0 \text{ MHz}$ in the inhomogeneously broadened absorption line.

C. Experimental setup

To excite the ${}^7F_0 \rightarrow {}^5D_0$ transition our experiment requires a light source providing a wavelength at around 580 nm, shown in Fig. 2. Unfortunately there are no commercial diode lasers at this wavelength. As a result dye lasers are commonly used,

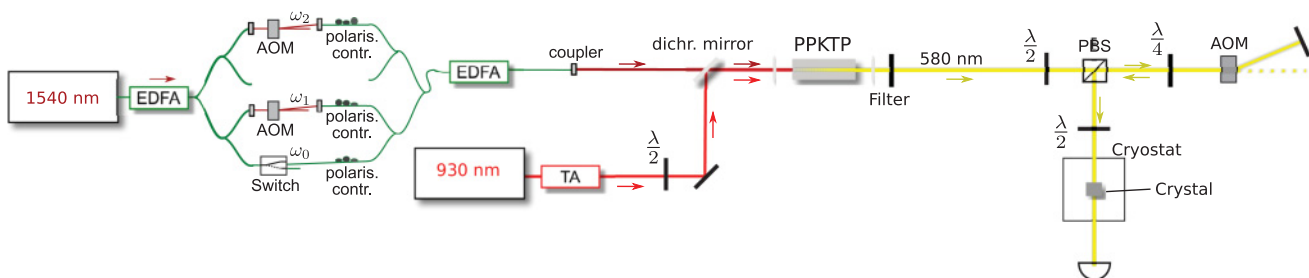


FIG. 2. (Color online) Experimental setup. The core of the setup is the periodically poled potassium titanyl phosphate (PPKTP) waveguide which is pumped with two external cavity diode lasers at 930 and 1540 nm, respectively. The nonlinear properties of the waveguide enable the input light to be converted into light at 580 nm using sum-frequency generation. AOM, acousto-optical modulators; EDFA, erbium-doped fiber amplifier; TA, tapered amplifier; PBS, polarizing beam splitter. $\lambda/2$ and $\lambda/4$ denote half- and quarter-wave plates, respectively.

but they are bulky and are difficult to stabilize in frequency. In this work we have developed a source based on sum-frequency generation (SFG) of two cw external-cavity diode lasers, at 930 and 1540 nm, in a nonlinear crystal. To increase the efficiency of the SFG process we used a periodically poled potassium titanyl phosphate (PPKTP) crystal with a waveguide channel on its surface. In this way one can still make use of the advantages of compact diode lasers, especially concerning the straightforwardness of frequency stabilization.

To reach sufficient power levels at 580 nm both pump lasers were amplified using two erbium-doped fiber amplifiers (EDFAs) for 1540 nm and a tapered amplifier for 930 nm, respectively. A telescope for each infrared laser improved the mode matching of the incoupled light to the waveguide. The KTP crystal was cooled down to a temperature of approximately 16 °C to reach the phase-matching condition. To filter out residual infrared light after the SFG we used two dichroic mirrors with high reflectivity at 580 nm placed right after the KTP crystal.

To address the different hyperfine transitions in $\text{Eu}^{3+}:\text{Y}_2\text{SiO}_5$ (see Fig. 1) we used two pulsed acousto-optical modulators (AOMs) as frequency shifters and a pulsed fiber-optical switch at 1540 nm. In this way we could produce up to three pulsed beams at different fixed frequencies. In addition, by slight realignment of the AOMs we could change the frequencies enough to address other hyperfine transitions. The three 1540-nm beams were combined in a single-mode fiber using fiber-based beam combiners. Note that the most powerful EDFA was placed after the last beam combiner, which has the great advantage of making the 580-nm output virtually independent of losses before the EDFA, since the amplifier could easily be saturated under all experimental conditions presented in this paper. Note that the 930-nm laser ran in cw mode during all experiments. Another AOM in double-pass configuration at 580 nm allowed for additional small frequency shifts (order of 10 MHz) and variable amplitude modulation. All AOMs were controlled using arbitrary function generators and a digital output card.

The light modulated by the double-pass AOM at 580 nm was then sent into the crystal sample mounted on the cold finger of a pulse tube cooler at a temperature of 2.6 K. The transmitted signal was detected with a photodiode.

With this setup we reached a power at 580 nm of up to $P_{580} = 110$ mW (in cw mode), with $P_{930} \approx 355$ mW and $P_{1540} \approx 1455$ mW (in cw mode) measured before the incoupling lens (which was antireflection coated for 930 nm). By comparing power at 930 nm transmitted through the waveguide with and without injecting light from the laser at 1540 nm, we calculate that 75.5% of the light at 930 nm inside the PPKTP waveguide gets converted into light at 580 nm. From these numbers we estimate a coupling efficiency of $\eta_{930} < 0.26$; thus, better mode matching of the 930-nm laser could further increase the 580-nm power output.

III. SPECTROSCOPIC MEASUREMENTS

A. Determining the order of the hyperfine levels

For the implementation of the AFC scheme with spin-wave storage it is important to address only one of the nine classes

of ions mentioned in Sec. II A. Otherwise an efficient transfer of the coherence to a ground-state spin level would be very difficult, if not impossible, since the transition would not possess a unique Rabi frequency. A π pulse for one class of ions would mean a different angle on the Bloch sphere for the other classes and thus only a partial transfer of the coherence. To choose the right frequencies to address only one class, it is necessary to know the order of the hyperfine levels in the ground and in the excited states.⁴⁷

The hyperfine splitting in the 5D_0 excited state is determined by the pure quadrupole interaction, whereas in the 7F_0 ground state there are two contributions: the pure quadrupole interaction and a so-called pseudoquadrupole interaction.⁴⁶ The latter is a second-order magnetic hyperfine interaction acting through the 7F_1 level found at $200+$ cm^{-1} above the ground state. The canceling effect of two mechanisms can change the ordering of the hyperfine components compared to that given by the pure quadrupole term.

To determine the order of the ground-state levels we used two different methods. The first is based on a dual-frequency hole burning technique developed by Nilsson *et al.*⁴⁷ The other uses directly the information contained in the single-frequency hole burning spectrum, by comparing to a theoretical model. This latter method can also give information on the relative strengths of the optical-hyperfine transitions.

For the first method, suppose we shine light at two different frequencies into the sample, where the difference $\Delta\omega$ matches one of the ground-state splittings (90 MHz or 119 MHz in $^{153}\text{Eu}^{3+}:\text{Y}_2\text{SiO}_5$; cf. Fig. 1). Then an asymmetry will occur in the hole burning spectrum. Depending on the ordering of the ground-state hyperfine levels, certain antiholes will be enhanced on one side of the central frequency with respect to their counterpart on the other side. This is, in short, due to the fact that for classes of ions which are in resonance with the two frequencies, ions will be pumped into the third ground state, leading to enhanced absorption from this state. Note, however, that in practice this asymmetry can be difficult to observe due to a difference in the strength of the contributing transitions.

Figure 3(b) shows a hole burning spectrum for $\Delta\omega = 90$ MHz. One can clearly see an asymmetry in the spectrum. For the ordering given in Fig. 1, one would expect an enhancement of the antihole at a frequency of 119 MHz. In comparison with Fig. 3(a) there is indeed a significantly increased absorption for the antihole at this position. However, the same is the case for the antihole at -209 MHz, which would indicate the inverse ordering.

A simulation of the hole burning spectrum showed that one should observe an enhanced absorption also at -335 MHz and -75 MHz, which correspond to other transitions originating from the $|\pm 5/2\rangle_g$ level. This enhancement should not occur for the inverse order. The particular enhancement pattern that we observe is only compatible with the ground-state ordering shown in Fig. 1.

The enhanced absorption at -209 MHz is due to an overlap of two antiholes stemming from two independent single-frequency burning spectra separated by $\Delta\omega = 90$ MHz. The absence of strong enhancements that should occur at other frequencies can be explained by the small transition strength of the corresponding hyperfine transitions.

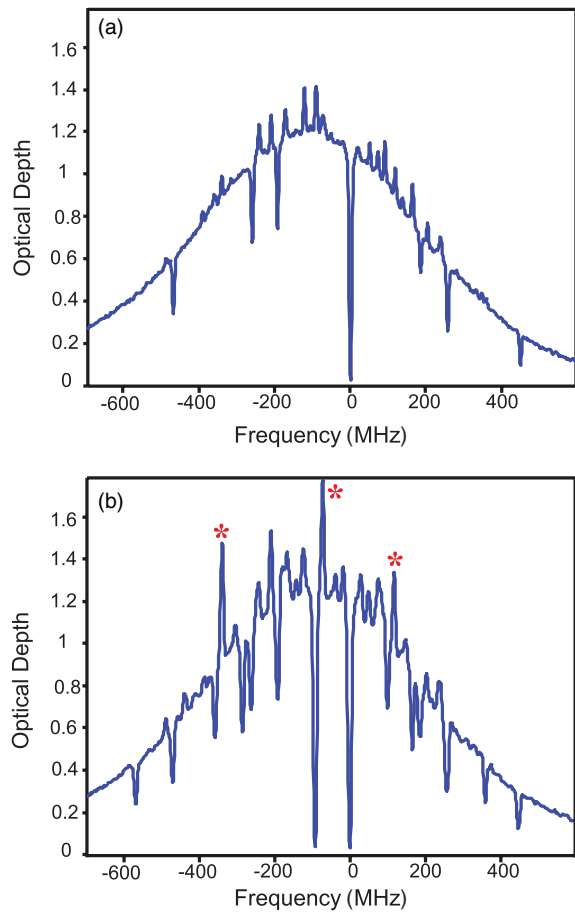


FIG. 3. (Color online) Spectral hole burning spectra of $^{153}\text{Eu}^{3+}\text{Y}_2\text{SiO}_5$. (a) Light at a single frequency was shone into the sample. One can clearly see the central spectral hole at the laser frequency (here at 0 MHz), as well as side holes at the hyperfine level spacings of the excited state [at approximately ± 194 MHz, ± 260 MHz, and $\pm(194 \text{ MHz} + 260 \text{ MHz}) = \pm 454$ MHz]. The peaks (antiholes) are due to an enhanced population in ground-state levels not addressed by the laser. The different sizes of the side and antiholes are due to differences in the strengths of the respective hyperfine transitions. (b) Light at two frequencies (0 and -90 MHz) with a frequency difference corresponding to the level spacing between $|\pm 1/2\rangle_g$ and $|\pm 3/2\rangle_g$ (90 MHz) is shone into the sample. For three classes of ions all the population is transferred to $|\pm 5/2\rangle_g$. This leads to strong asymmetry in the hole burning spectrum which indicates the ordering of the hyperfine levels in the ground state. The stars show the antiholes at -335 , -75 , and 119 MHz where a particularly strong enhancement is observed, allowing us to determine the ground-state order (see text). Note that the frequency scan of the laser used to read out the absorption was not perfectly linear such that the positions of some of the (anti)holes may occur slightly shifted.

We performed the same measurement for the other hyperfine level spacing of $\Delta\omega = 119$ MHz. A comparison with simulations indicated the same ordering.

The second method uses hole burning spectra recorded with a single burning frequency which are compared to a theoretical model with appropriate transition probabilities as shown in Fig. 4. Indeed, under suitable experimental conditions, a surprising amount of information about the individual

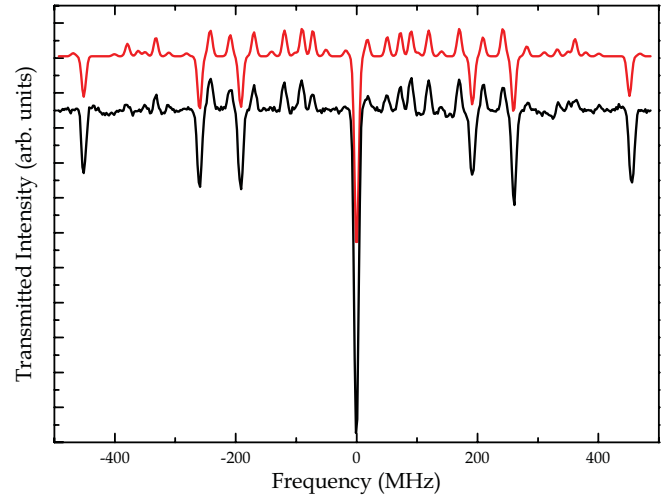


FIG. 4. (Color online) Experimental hole burning spectrum (lower curve) recorded using a single burn frequency compared with a simulation (upper curve) using the transition probabilities listed in Table I (see text for details). The measured and simulated holes on the far right do not align because the measured hole position was shifted by an uncorrected nonlinearity of the frequency scan. The spectra are normalized to the absorption line shapes.

optical-hyperfine transitions can be gathered from analysis of observed asymmetry in antihole intensities in hole burning spectra for inhomogeneously broadened lines. That analysis, including intensity asymmetry on opposite sides of the central hole, provides an alternate route for determining the order of the hyperfine levels in both the ground and the excited states and also the relative transition probabilities.

The intensity observed for a specific antihole h_{ijkl} (or specific contribution, for the three cases where three transitions participate in single antiholes), between ground-state level k and excited-state level l , is related linearly to a product of the excess population n_{ijk} in k due to the burning transition from level i to level j and the transition probability for reading γ_{kl} , i.e., $h_{ijkl} \propto n_{ijk}\gamma_{kl}$. If one assumes equal $1/3$ branching during decay from the excited state j to all ground-state hyperfine levels, as a consequence of the many pathways of the cascading decay through $48\ ^7F_j$ levels, the excess population is given by $n_{ijk} \propto 1/3 N_i (1 - \exp(-\gamma_{ij}t))$, where N_i is the initial population in i before burning and t is the burn time. We can further assume that all ground-state levels are initially equally populated $N_i = 1/3$. The antihole intensity then simplifies to $h_{ijkl} \propto (1 - \exp(-\gamma_{ij}t))\gamma_{kl}$.

The asymmetry in the amplitude of the antiholes requires that a deep central hole be burned ($\gamma_{ij}t \gg 1$). Antiholes that correspond to a strong transition during burning and a weak transition during reading have smaller amplitudes compared to the opposite case. Deep central holes are needed to obtain this asymmetry, ideally in which case $\gamma_{ij}t \gg 1$ such that $h_{ijkl} \propto \gamma_{kl}$. If the burning is shallow ($\gamma_{ij}t \ll 1$), expanding the exponential factor simplifies the expression, giving $h_{ijkl} \propto \gamma_{ij}\gamma_{kl}$. In that shallow-burning limit, the hole pattern becomes symmetric since $h_{ijkl} = h_{klij}$.

The considerations described above were incorporated in a computer program. A simple least-squares-fitting procedure was used to deduce the relative transition probabilities. Six

TABLE I. Fitted transition probabilities γ_{ij} between hyperfine states of 7F_0 and 5D_0 from analysis of hole burning spectra. Uncertainty in each probability is estimated to be about ± 0.05 .

	$ \pm 1/2\rangle_e$	$ \pm 3/2\rangle_e$	$ \pm 5/2\rangle_e$
$ \pm 1/2\rangle_g$	0.11	0.16	0.73
$ \pm 3/2\rangle_g$	0.16	0.66	0.18
$ \pm 5/2\rangle_g$	0.73	0.18	0.09

parameters were used: a proportionality constant, a burning time t , and four independent transition probabilities γ_{ij} . Only four transition probabilities are needed since each row and column listing the probabilities should add to 1. For ${}^{153}\text{Eu}^{3+}:\text{Y}_2\text{SiO}_5$, there is no requirement of a symmetric array, since these transitions are between ground- and excited-state hyperfine levels and the principal axes for each level can in principle be different since they are not constrained by symmetry.

Of the four possible relative orderings of hyperfine levels in 7F_0 and 5D_0 , only the one shown in Fig. 1 proved to give a good representation of the experimentally measured spectrum of Fig. 4. Only antiholes were used in the fitting, since they are more sensitive to the individual transition probabilities. The best fit, shown in the upper curve in Fig. 4, was achieved with the transition probabilities listed in Table I. Those transition probabilities were found using a γ_{ijt} of 5.0 for the strongest burning transition. The transition probabilities were found to be symmetric, though this was not required in the fitting procedures.

In Sec. III B we use another method, presumably more direct and precise, for measuring the relative transition strengths (compare to Table II). The agreement found between the two methods gives additional credence to the assumptions on which the analysis presented in this section is based.

B. Spectral tailoring sequence

The main goal of this work is the identification of a Λ system in ${}^{153}\text{Eu}^{3+}:\text{Y}_2\text{SiO}_5$ which is suitable for quantum applications. As mentioned in the introduction, this requires the application of elaborate spectral tailoring techniques. In the following we explain the experimental cycle which allows for an adequate preparation of the absorption profile. This is the basis for future work on the AFC scheme with spin-wave storage. Here we use the prepared absorption profile to confirm the order of the hyperfine levels, to directly measure the relative transition strengths, and to measure the Rabi frequency of one optical-hyperfine transition.

TABLE II. Relative transition probabilities γ_{ij} for ${}^{153}\text{Eu}^{3+}:\text{Y}_2\text{SiO}_5$ extracted from hole burning spectra as described in Sec. III C. Uncertainty in each probability is estimated to be about ± 0.03 .

	$ \pm 1/2\rangle_e$	$ \pm 3/2\rangle_e$	$ \pm 5/2\rangle_e$
$ \pm 1/2\rangle_g$	0.03	0.22	0.75
$ \pm 3/2\rangle_g$	0.12	0.68	0.20
$ \pm 5/2\rangle_g$	0.85	0.10	0.05

To select an individual class of ions, one can apply the pump laser at three frequencies simultaneously.⁴⁷ These frequencies have to be chosen such that only for the chosen class all three ground-state levels are coupled to at least two different excited-state levels. The population of this class is redistributed among the three ground-state levels. For all other classes there is at least one ground-state level that is not addressed by the three frequencies. The population of these classes is completely transferred to this level. By sweeping the laser frequency during optical pumping, one can achieve this over a certain spectral region around the chosen frequencies which is only limited by the level spacings. The population of all other classes can be found outside of these spectral regions.

In practice, we applied spectral tailoring sequences as illustrated in Fig. 5 for a range of different combinations of pump frequencies. By testing several potential Λ systems we could extensively test the order we had previously determined and could gather more accurate data on relative optical-hyperfine transition strengths. These frequencies were chosen such that, for the hyperfine level order in Fig. 1, we only addressed one of the nine classes of ions. Two of the transitions formed a Λ system and the third one connected the remaining ground-state level to one of the unused excited-state levels as shown in the example in Fig. 5(d). This is necessary in order to remove classes in which only the excited-state levels are shifted by the inhomogeneous broadening.

At first, light at all three frequencies was alternately sent into the sample [Fig. 5(a)]. As described above, ions will be redistributed between the three ground-state levels of this class, while other ions are pumped away. We call this part of the sequence *class cleaning*.

After the class cleaning sequence we have a flat nonzero absorption in all three spectral pits, originating only from

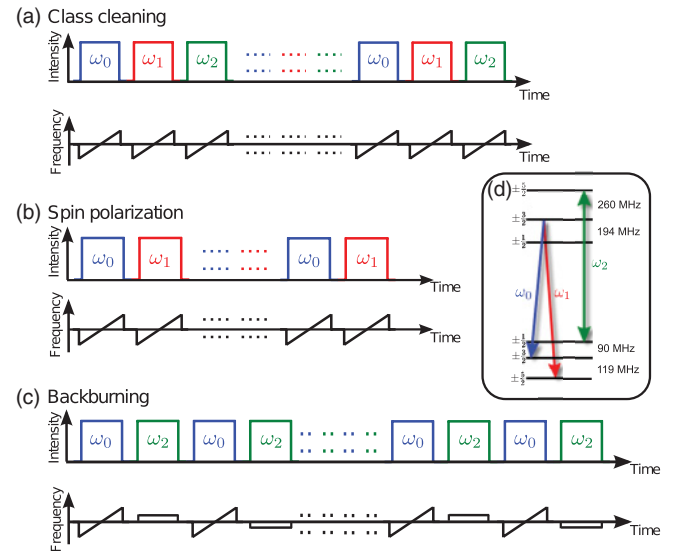


FIG. 5. (Color online) The optical pump sequence used for preparing and manipulating the population of a particular class of ions within the inhomogeneous broadening. As explained in more detail in the text the sequence consists of (a) a class cleaning part, (b) a spin-polarization part, and (c) a peak backburning part. In (d) we show the Λ system used for the measurements presented in this paper.

the chosen class. To empty the ground-state levels of the Λ system [states $|\pm 3/2\rangle_g$ and $|\pm 5/2\rangle_g$ in the example shown in Fig. 5(d)], light at the corresponding frequencies (ω_0 and ω_1) is again alternately sent into the sample and the laser frequency is swept; see Fig. 5(b). The population of the chosen class will be spin-polarized into the third ground-state level [state $|\pm 1/2\rangle_g$ in Fig. 5(d)]. We call this part of the sequence *spin polarization*.

To create absorption peaks in the empty pits, ions are moved back by shining light at ω_2 on the sample (now without sweeping the laser frequency). We call this part of the sequence *backburning* [Fig. 5(c)]. This produces a narrow spectral hole at ω_2 and narrow antiholes (peaks) at ω_0 and ω_1 . During the application of light at ω_2 , an additional frequency offset, which is small compared to the pit width, determines the position of the peaks inside the pits. By applying this sequence using several different frequency offsets, one can create combs. To obtain an absorption peak in only one of the pits, e.g., the one at ω_1 , one can remove the population after each backburn pulse from the other pit by shining light at ω_0 while sweeping the laser frequency.

C. Spectral tailoring results

In Fig. 6 we show absorption spectra after application of the hole burning sequence described above with $\omega_1 = \omega_0 + 119$ MHz and $\omega_2 = \omega_0 + 170$ MHz [see also Fig. 5(d)]. In Fig. 6(a) we backburn at ω_2 and we optically pump at ω_0 , while sweeping the laser, to spin-polarize the population into state $|\pm 5/2\rangle_g$. Since we here applied backburning at two different frequencies, separated by about 5 MHz, one can observe two absorption peaks in the spectral pit at ω_1 . In Fig. 6(b) we apply the same hole burning sequence, with the only difference that we optically pump at ω_1 , instead of at ω_0 , while backburning. This results in a spin polarization in state $|\pm 3/2\rangle_g$ as shown by the two absorption peaks in the pit at ω_0 . Note that for both examples one can observe the corresponding spectral holes at the frequencies where we applied the backburn laser (around ω_2).

Furthermore, in Fig. 6(a) we can see two peaks on an absorbing background around $\omega_0 - 75$ MHz. These peaks disappear if we move the population into $|\pm 3/2\rangle_g$, as can be seen in Fig. 6(b). The transition $|\pm 5/2\rangle_g \rightarrow |\pm 1/2\rangle_e$ in Fig. 5(d) is at $\omega_0 - 75$ MHz. We thus attribute these peaks to the population in $|\pm 5/2\rangle_g$.

If the order of the hyperfine levels in the excited state in Fig. 1(d) was not the correct one, we should not observe peaks at $\omega_0 - 75$ MHz. However, in that case these peaks might also be due to an imperfect class cleaning procedure. We therefore compared the hole burning spectra with a set of simulations of the hole burning sequence we carried out for all different combinations of the orders in ground and excited states. Only for the order shown in Fig. 1 could we observe peaks in this region. We repeated this comparison for different Λ systems in different classes by addressing different transitions. The results confirmed our assumptions and are in agreement with what we have found in the measurements presented in Sec. III A.

We can, in principle, also use the absorption depths of peaks and holes created during the spectral tailoring sequence to

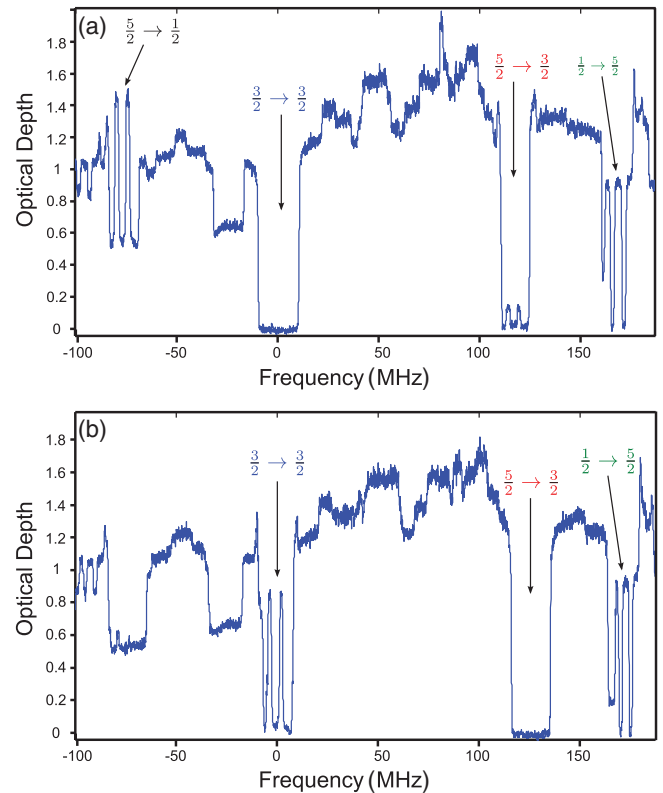


FIG. 6. (Color online) Absorption spectra after running the preparation scheme described in Sec. III B. The transitions used are those illustrated in Fig. 5. The horizontal scale refers to frequency shifts relative to ω_0 . The relevant transitions of the prepared spectral regions are indicated. The scan of the laser was somewhat nonlinear. (a) Two absorption peaks are prepared on $|\pm 5/2\rangle_g$ of the selected class of ions. They appear in the spectral pit around $\omega_0 + 119$ MHz on the $|\pm 5/2\rangle_g \rightarrow |\pm 3/2\rangle_e$ transition as well as around $\omega_0 - 75$ MHz on the $|\pm 5/2\rangle_g \rightarrow |\pm 1/2\rangle_e$ transition. (b) Two absorption peaks are prepared on $|\pm 3/2\rangle_g$.

determine the relative optical-hyperfine transition strengths. Since we are dealing here with a single class of ions, the interpretation should be more straightforward than the analysis performed on single-frequency hole burning spectra presented in Sec. III A. In Fig. 6 one can clearly see that the transitions $|\pm 3/2\rangle_g \rightarrow |\pm 3/2\rangle_e$ (at ω_0) and $|\pm 1/2\rangle_g \rightarrow |\pm 5/2\rangle_e$ (at $\omega_0 + 170$ MHz) are of similar strength since the holes and peaks are of similar optical depth, while the transition $|\pm 5/2\rangle_g \rightarrow |\pm 3/2\rangle_e$ (at $\omega_0 + 119$ MHz) is significantly weaker. The optical depth is proportional to the strength of the transition and the number of ions in the ground state. As a result it is very important that, for all spectra used in the analysis, the same number of ions populate the ground state. Since our analysis involved spectra taken at different experimental conditions of a longer period of time, this is not a viable assumption due to variations in experimental parameters such as frequency drifts and power fluctuations of the laser as well as a nonlinearity of the readout scan. Furthermore, the number of ions also depends on the laser position within the inhomogeneously broadened profile.

To minimize this error, we chose another way to access information about the relative transition strengths. Knowing

that the peaks at $\omega_0 - 75$ MHz and $\omega_0 + 119$ MHz in Fig. 6(a) belong to the same ground-state level of a unique class, the contributing number of ions has to be the same for both. We can thus use the height of these peaks to calculate the ratio of the strength of transition $|\pm 5/2\rangle_g \rightarrow |\pm 1/2\rangle_e$ (at $\omega_0 - 75$ MHz) to transition $|\pm 5/2\rangle_g \rightarrow |\pm 3/2\rangle_e$ (at $\omega_0 + 119$ MHz). Note that we are using a single readout (i.e., no averaging) of the absorption spectrum to obtain this information. We have applied this method to a range of different combinations of pump frequencies, involving different Λ systems. These measurements were then used to assess all relative transition probabilities in $^{153}\text{Eu}^{3+}:\text{Y}_2\text{SiO}_5$.

To estimate the relative transition strengths γ_{ij} of all transitions $i \rightarrow j$ we used several measured ratios γ_{ij}/γ_{ik} (with a common initial state i). We further used the fact that summing probabilities should yield $\sum_{j=1,3,5} \gamma_{ij} = 1$ for all $i = 1, 3, 5$, resulting in four independent parameters γ_{ij} (see Sec. III A). This gives a set of equations that we use in a fitting procedure to extract the transition strengths γ_{ij} that yield the best fit with all measured ratios. The result is listed in Table II. Some of the absorption peaks used to evaluate the transition ratios were small (around 10% absorption, like the peaks in the $|\pm 5/2\rangle_g \rightarrow |\pm 3/2\rangle_e$ transition in the example above). The measured optical depths of these peaks thus still contain a large uncertainty. By increasing the number of measurements (Λ systems), we tried to further minimize the uncertainty of our results. The results shown in Table II generally agree with those presented in Table I, within the experimental errors. But it is worth noting that the results shown in Table II display an asymmetry.

D. The choice of a Λ system

In a Λ system two ground-state levels have to be efficiently coupled to the same excited-state level. One should thus pick the two strongest transitions of a column of Table II. We can see that there are two candidates which are approximately equally well suited, one using $|3/2\rangle_e$ and one using $|5/2\rangle_e$. Note that, in order to address a unique class of ions, the third transition used for state preparation should couple the remaining ground-state level to one of the two unused excited-state levels; i.e., it should belong to a different column than the Λ transitions.

IV. RABI FREQUENCY MEASUREMENT

For the complete AFC scheme one must achieve coherent and efficient transfer of an excitation using an optical control pulse.^{21,36} This could be done with a fast π pulse or a more sophisticated chirped adiabatic pulse. The latter can transfer a larger spectral bandwidth, which is important in the context of the AFC scheme.⁴⁸ In both cases, the performance of the control pulse depends strongly on the achievable Rabi frequency under realistic conditions in terms of optical power and the focus diameter in the crystal. In this section we present measurements of the Rabi frequency on the $|3/2\rangle_g \rightarrow |3/2\rangle_e$ transition. These measurements also allow us to deduce the dipole moment. Using the results presented in Sec. III one can calculate the dipole moment of the other eight hyperfine transitions.

The Rabi frequency measurements on the $|3/2\rangle_g \rightarrow |3/2\rangle_e$ transition were carried out using a method similar to the one presented in Ref. 47. We first selected a single class of ions using the spectral tailoring sequence described in Sec. III B. But instead of preparing peaks we created a flat absorption structure in the spectral pit at frequency ω_0 . Thus, all ions of the class are pumped into the ground state $|3/2\rangle_g$, that is $\rho_g = 1$, while the excited state $|3/2\rangle_e$ was emptied, $\rho_e = 0$ (note that total population is normalized to 1, $\rho_g + \rho_e = 1$). After this state initialization we applied a strong resonant pulse of duration τ at the center of the spectral pit. This Rabi pulse coherently drives the ions toward the excited state with a rate Ω_R that is proportional to the dipole moment μ_{ge} and the electrical field amplitude E , $\Omega_R = \mu_{ge}E/\hbar$.⁴⁹ In absence of decoherence the state vector $\vec{r} = (r_1, r_2, r_3)$ will be rotated by an angle $\theta = \Omega_R\tau$ on the Bloch sphere. By measuring the population inversion $r_3 = \rho_e - \rho_g$ one can observe Rabi flopping between the ground state, $r_3 = -1$, and the excited state, $r_3 = 1$. Experimentally the population inversion can be calculated from the ratio of the resonant optical depth d measured after the Rabi pulse, to the initial optical d_0 measured before applying the Rabi pulse, that is, $r_3 = -d/d_0$. We measure the optical depth by simply recording the absorption spectrum using a weak readout pulse during which the laser frequency is scanned over the range of the pit.

The experimental setup was somewhat modified with respect to the setup shown in Fig. 2. The laser was frequency locked to a cavity at 580 nm, using a Pound-Drever-Hall configuration.⁵⁰ This reduced drifts of the laser frequency and narrowed the laser linewidth to <100 kHz. The AOM at 580 nm was used in a single-pass configuration in order to maximize the power arriving at the crystal. The maximum power incident on the crystal was around 85 mW. The light was focused down to $50 \mu\text{m}$ (full width at half maximum).

Figure 7 shows absorption profiles recorded after applying Rabi pulses of four different durations. In Fig. 7(b) one can clearly observe optical gain, since there the measured optical depth reaches negative values, i.e., $r_3 > 0$. In Fig. 8 we plot an example of the population inversion as a function of the duration of the Rabi pulse, for an incident power of approximately 52 mW. One can clearly see an oscillatory behavior, which is proof of coherent driving of the ions. The population inversion shown in Fig. 8 is calculated from the optical depth measured at resonance (at zero frequency in Fig. 7). Off-resonant oscillations are not considered. A limitation in the accuracy of the determination of the Rabi frequency is the strong damping of the oscillations. This can be attributed to decoherence and propagation effects, as well as inhomogeneities in longitudinal and transverse directions of the electric field inside the crystal. Since these factors depend strongly on the experimental configuration, it is very difficult to find an analytical function that reproduces the data. Also, a comparison with one-dimensional Maxwell-Bloch simulations using a least-squares method did not lead to a satisfactory result. While in this model we could include both decoherence and propagation effects, the divergence of the beam as well as its transversal distribution was not taken into account.

To estimate the electric dipole moment of the transition from our data, we used the point $r_3 = 0$ where an angle of $\pi/2$ is reached on the Bloch sphere, indicated by the

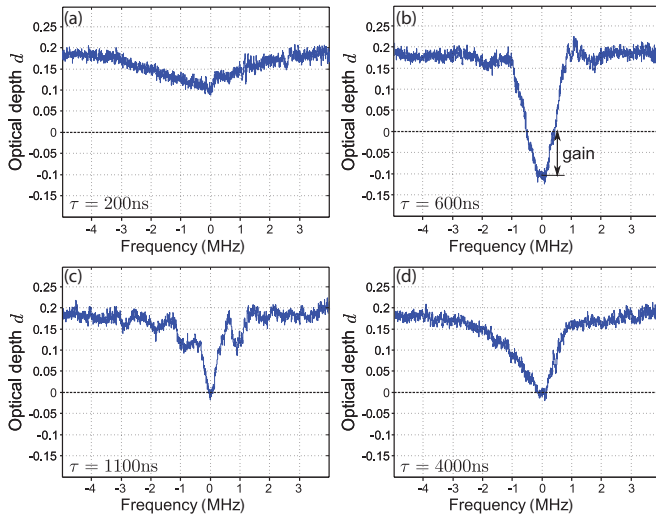


FIG. 7. (Color online) Absorption spectra measured after application of optical pulses of different durations τ on the $|3/2\rangle_g \rightarrow |3/2\rangle_e$ transition. Initially a flat absorption profile is prepared using the spectral hole burning technique described in Sec. III B. (a) A short Rabi pulse slightly reduces the absorption (zero frequency) since ions are moved to the excited state. (b) For $\tau = 600$ ns the optical depth is negative at resonance and optical gain is observed since $r_3 > 0$. (c) For even longer pulse durations the population is coherently driven back, increasing the optical depth. (d) Owing to the damping effects described in the text, an incoherent mixture state ($r_3 = 0$) is reached for $\tau \gtrsim 4$ μs , where the medium becomes completely transparent at resonance.

dashed line in Fig. 8. The Rabi frequency (in hertz) can then be calculated directly from the duration τ where $r_3 = 0$ is reached; $\Omega_R/2\pi = 1/4\tau$. The inset of Fig. 8 shows the Rabi frequency as a function of the electric field amplitude E , corresponding to different optical power P . Note that $E = \sqrt{(2P/A n \epsilon_0 c)}$, where the refractive index $n = 1.8$, A is the area of the focus, ϵ_0 is the dielectric constant, and c is the velocity of light.⁴⁹ The maximum Rabi frequency that we could obtain with this experimental configuration was around 600 kHz. From the slope of the fitted line we calculate an electric dipole moment of $\mu_{eg} = (5.0 \pm 0.1) \times 10^{-33}$ C m which corresponds to an oscillator strength of ($f = 3.08 \pm 0.01$) $\times 10^{-8}$ for the $|3/2\rangle_g \rightarrow |3/2\rangle_e$ transition. The errors given are the errors from the linear fit. We emphasize that due to the strong damping, however, it is likely that our measurement underestimates the actual oscillator strength. The strengths of the other transitions can be estimated using the relative transition probabilities presented in Tables I and II. Note that the relative transition probabilities in the tables are proportional to μ_{eg}^2 . We also carried out Rabi measurements for the $|5/2\rangle_g \rightarrow |3/2\rangle_e$ and the $|1/2\rangle_g \rightarrow |5/2\rangle_e$ transitions. For the former weak transition, the measurement uncertainty was large due to the low optical depth and the strong damping. In general, however, the periodicities of the observed oscillations are consistent with the results presented in Table II.

It should also be mentioned that an oscillator strength of $f = 1.3 \times 10^{-8}$ was found by K niz *et al.*³⁹ That value was obtained from the inhomogeneous absorption profile, i.e., without the distillation of a unique transition. It is thus an

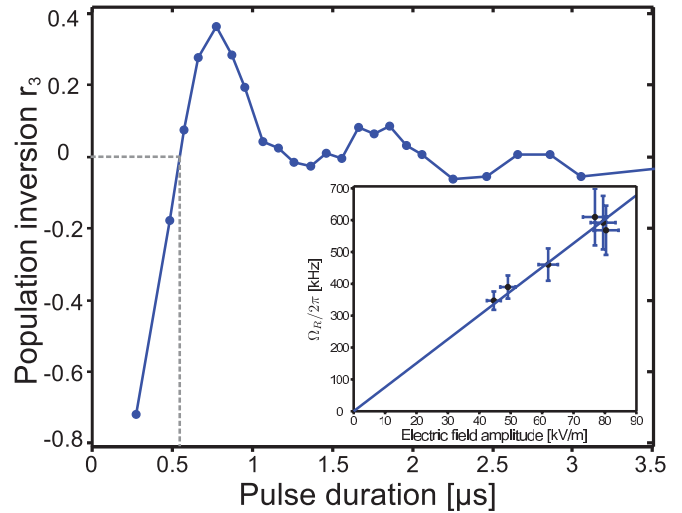


FIG. 8. (Color online) Population inversion r_3 as a function of the Rabi pulse duration, for a pulse peak power of 52 mW. The atomic population is oscillating as a consequence of coherent driving of the ions. However, due to decoherence and inhomogeneities the oscillation is strongly damped. The inset shows the Rabi frequency $\Omega_R/2\pi$ as a function of the electric field amplitude. $\Omega_R/2\pi$ was estimated by using the point where an angle of $\theta = \pi/2$ is reached on the Bloch sphere, i.e., $r_3 = 0$, as indicated by the dashed line in the main figure. From the slope of the graph in the inset we estimated the electric dipole moment of the transition to be $\mu_{eg} = (5 \pm 0.1) \times 10^{-33}$ C m. Note that in our experimental configuration an optical power of 52 mW corresponds to an electric field amplitude of 62 kV/m along the crystal D_1 direction. The transition dipole moment quoted above is thus a projection along D_1 .³⁹

average over all the hyperfine transitions, whereas here we measure the strength of a specific optical-hyperfine transition.

V. CONCLUSIONS

We have presented a detailed analysis of the hole burning spectrum of $^{153}\text{Eu}^{3+}:\text{Y}_2\text{SiO}_5$. From this analysis we could determine the order, in energy, of the hyperfine levels within the 7F_0 ground state and 5D_0 excited state. We could also obtain the relative strengths of the optical-hyperfine transitions. Using these results one can identify a suitable Λ system applicable in quantum applications such as quantum memories. We have also established spectral tailoring techniques for the distillation of a unique class of ions in the material. In particular, the hole burning techniques presented here allow one to prepare the spectrum as is required for the realization of the AFC quantum memory protocol including spin-wave storage. Demonstration of Rabi oscillations further shows that a coherent population transfer necessary for spin-wave storage should be feasible in $^{153}\text{Eu}^{3+}:\text{Y}_2\text{SiO}_5$. The spectroscopic results presented here will be highly useful in future work on quantum memories in $^{153}\text{Eu}^{3+}:\text{Y}_2\text{SiO}_5$.

ACKNOWLEDGMENTS

Y.S., R.M.M., and R.L.C. are grateful to R. Hutchison and R. W. Equall for growing the isotopically pure $^{153}\text{Eu}^{3+}$ -doped Y_2SiO_5 crystal. B.L., N.T., N.G., M.A., and H.d.R. thank Claudio Barreiro for technical assistance and would like

to thank N. Sangouard for useful discussions. The work conducted at the University of Geneva was supported by the Swiss NCCR-QP, NCCR-QSIT, and by the European projects QuRep, Q-Essence, ERC-Qore, and CIPRIS (FP7

Marie Curie Actions). Research at the Department of Physics, Montana State University, was supported in part by the US Air Force Research Laboratory under Agreement No. F49620-01-1-0313.

*mikael.afzelius@unige.ch

- ¹A. I. Lvovsky, B. C. Sanders, and W. Tittel, *Nat. Photonics* **3**, 706 (2009).
- ²K. Hammerer, A. S. Sørensen, and E. S. Polzik, *Rev. Mod. Phys.* **82**, 1041 (2010).
- ³C. Simon, M. Afzelius, J. Appel, A. Boyer de la Giroday, S. J. Dewhurst, N. Gisin, C. Y. Hu, F. Jelezko, S. Kröll, J. H. Müller, J. Nunn, E. S. Polzik, J. G. Rarity, H. De Riedmatten, W. Rosenfeld, A. J. Shields, N. Sköld, R. M. Stevenson, R. Thew, I. A. Walmsley, M. C. Weber, H. Weinfurter, J. Wrachtrup, and R. J. Young, *Eur. Phys. J. D* **58**, 1 (2010).
- ⁴W. Tittel, M. Afzelius, T. Chanelière, R. L. Cone, S. Kröll, S. Moiseev, and M. Sellars, *Laser Photonics Rev.* **4**, 244 (2010).
- ⁵H.-J. Briegel, W. Dür, J. I. Cirac, and P. Zoller, *Phys. Rev. Lett.* **81**, 5932 (1998).
- ⁶L.-M. Duan, M. D. Lukin, J. I. Cirac, and P. Zoller, *Nature (London)* **414**, 413 (2001).
- ⁷N. Sangouard, C. Simon, H. de Riedmatten, and N. Gisin, *Rev. Mod. Phys.* **83**, 33 (2011).
- ⁸B. Julsgaard, J. Sherson, J. I. Cirac, J. Fiurášek, and E. S. Polzik, *Nature (London)* **432**, 482 (2004).
- ⁹T. Chanelière, D. N. Matsukevich, S. D. Jenkins, S.-Y. Lan, T. A. B. Kennedy, and A. Kuzmich, *Nature (London)* **438**, 833 (2005).
- ¹⁰M. D. Eisaman, A. André, F. Massou, M. Fleischhauer, A. S. Zibrov, and M. D. Lukin, *Nature (London)* **438**, 837 (2005).
- ¹¹K. S. Choi, H. Deng, J. Laurat, and H. J. Kimble, *Nature (London)* **452**, 67 (2008).
- ¹²K. F. Reim, J. Nunn, V. O. Lorenz, B. J. Sussman, K. C. Lee, N. K. Langford, D. Jaksch, and I. A. Walmsley, *Nat. Photonics* **4**, 218 (2010).
- ¹³M. Hosseini, B. Sparkes, G. Campbell, P. Lam, and B. Buchler, *Nat. Commun.* **2**, 174 (2011).
- ¹⁴M. Hosseini, G. Campbell, B. M. Sparkes, P. K. Lam, and B. C. Buchler, *Nat. Phys.* **7**, 794 (2011).
- ¹⁵H. de Riedmatten, M. Afzelius, M. U. Staudt, C. Simon, and N. Gisin, *Nature (London)* **456**, 773 (2008).
- ¹⁶M. P. Hedges, J. J. Longdell, Y. Li, and M. J. Sellars, *Nature (London)* **465**, 1052 (2010).
- ¹⁷E. Saglamyurek, N. Sinclair, J. Jin, J. A. Slater, D. Oblak, F. Bussières, M. George, R. Ricken, W. Sohler, and W. Tittel, *Nature (London)* **469**, 512 (2011).
- ¹⁸C. Clausen, I. Usmani, F. Bussières, N. Sangouard, M. Afzelius, H. de Riedmatten, and N. Gisin, *Nature (London)* **469**, 508 (2011).
- ¹⁹E. Fraval, M. J. Sellars, and J. J. Longdell, *Phys. Rev. Lett.* **95**, 030506 (2005).
- ²⁰J. J. Longdell, E. Fraval, M. J. Sellars, and N. B. Manson, *Phys. Rev. Lett.* **95**, 063601 (2005).
- ²¹M. Afzelius, C. Simon, H. de Riedmatten, and N. Gisin, *Phys. Rev. A* **79**, 052329 (2009).
- ²²S. A. Moiseev and S. Kröll, *Phys. Rev. Lett.* **87**, 173601 (2001).
- ²³M. Nilsson and S. Kröll, *Opt. Commun.* **247**, 393 (2005).
- ²⁴B. Kraus, W. Tittel, N. Gisin, M. Nilsson, S. Kroll, and J. I. Cirac, *Phys. Rev. A* **73**, 020302 (2006).
- ²⁵A. L. Alexander, J. J. Longdell, M. J. Sellars, and N. B. Manson, *Phys. Rev. Lett.* **96**, 043602 (2006).
- ²⁶C. Simon, H. de Riedmatten, M. Afzelius, N. Sangouard, H. Zbinden, and N. Gisin, *Phys. Rev. Lett.* **98**, 190503 (2007).
- ²⁷M. Bonarota, J. L. Le Gouët, and T. Chanelière, *New J. Phys.* **13**, 013013 (2011).
- ²⁸I. Usmani, M. Afzelius, H. de Riedmatten, and N. Gisin, *Nat. Commun.* **1**, 12 (2010).
- ²⁹M. Bonarota, J. Ruggiero, J.-L. Le Gouët, and T. Chanelière, *Phys. Rev. A* **81**, 033803 (2010).
- ³⁰A. Amari, A. Walther, M. Sabooni, M. Huang, S. Kroll, M. Afzelius, I. Usmani, B. Lauritzen, N. Sangouard, H. de Riedmatten, and N. Gisin, *J. Lumin.* **130**, 1579 (2010).
- ³¹M. Sabooni, F. Beaudoin, A. Walther, N. Lin, A. Amari, M. Huang, and S. Kröll, *Phys. Rev. Lett.* **105**, 060501 (2010).
- ³²B. S. Ham, M. S. Shahriar, and P. R. Hemmer, *Opt. Lett.* **22**, 1138 (1997).
- ³³K. Ichimura, K. Yamamoto, and N. Gemma, *Phys. Rev. A* **58**, 4116 (1998).
- ³⁴J. Klein, F. Beil, and T. Halfmann, *Phys. Rev. Lett.* **99**, 113003 (2007).
- ³⁵P. Goldner, O. Guillot-Noël, F. Beaudoux, Y. Le Du, J. Lejay, T. Chanelière, J.-L. Le Gouët, L. Rippe, A. Amari, A. Walther, and S. Kröll, *Phys. Rev. A* **79**, 033809 (2009).
- ³⁶M. Afzelius, I. Usmani, A. Amari, B. Lauritzen, A. Walther, C. Simon, N. Sangouard, J. Minar, H. de Riedmatten, N. Gisin, and S. Kröll, *Phys. Rev. Lett.* **104**, 040503 (2010).
- ³⁷R. Yano, M. Mitsunaga, and N. Uesugi, *J. Opt. Soc. Am. B* **9**, 992 (1992).
- ³⁸R. W. Equall, Y. Sun, R. L. Cone, and R. M. Macfarlane, *Phys. Rev. Lett.* **72**, 2179 (1994).
- ³⁹F. Könz, Y. Sun, C. W. Thiel, R. L. Cone, R. W. Equall, R. L. Hutcherson, and R. M. Macfarlane, *Phys. Rev. B* **68**, 085109 (2003).
- ⁴⁰R. Yano, M. Mitsunaga, and N. Uesugi, *Opt. Lett.* **16**, 1884 (1991).
- ⁴¹J. J. Longdell, A. L. Alexander, and M. J. Sellars, *Phys. Rev. B* **74**, 195101 (2006).
- ⁴²A. L. Alexander, J. J. Longdell, and M. J. Sellars, *J. Opt. Soc. Am. B* **24**, 2479 (2007).
- ⁴³M. Nilsson, L. Rippe, N. Ohlsson, T. Christiansson, and S. Kröll, *Phys. Scr. T* **T102**, 178 (2002).
- ⁴⁴M. Mitsunaga, R. Yano, and N. Uesugi, *Opt. Lett.* **16**, 264 (1991).
- ⁴⁵M. Mitsunaga, *Opt. Quantum Electron.* **24**, 1137 (1992).
- ⁴⁶R. M. Macfarlane and R. M. Shelby, in *Spectroscopy of Solids Containing Rare Earth Ions*, edited by A. A. Kaplinskii and R. M. Macfarlane (North Holland, Amsterdam, 1987), Chap. 3.
- ⁴⁷M. Nilsson, L. Rippe, S. Kröll, R. Klieber, and D. Suter, *Phys. Rev. B* **70**, 214116 (2004).
- ⁴⁸J. Minář, N. Sangouard, M. Afzelius, H. de Riedmatten, and N. Gisin, *Phys. Rev. A* **82**, 042309 (2010).
- ⁴⁹R. W. Boyd, *Nonlinear Optics* (Academic Press, San Diego, CA, 1992).
- ⁵⁰E. D. Black, *Am. J. Phys.* **69**, 79 (2001).